

Controlling the angular distribution of atomic photoelectrons in the region of laser-induced continuum structure in the femtosecond time domain

A N Grum-Grzhimailo^{1,2}, A D Kondorskiy³ and K Bartschat²

¹ Institute of Nuclear Physics, Moscow State University, Moscow 119992, Russia

² Department of Physics and Astronomy, Drake University, Des Moines, IA 50311, USA

³ P N Lebedev Physical Institute, Leninsky pr, 53, Moscow, 119991, Russia and Moscow Institute of Physics and Technology, Institutsky pr, 9, Dolgoprudny, Moscow Region, 141700, Russia

Received 9 June 2006, in final form 29 August 2006

Published 1 November 2006

Online at stacks.iop.org/JPhysB/39/4659

Abstract

The influence of laser-induced continuum structure on the angular distribution of photoelectrons is studied in the femtosecond time domain by direct numerical solution of the time-dependent Schrödinger equation. Control of the photoelectron angular distribution is demonstrated for the hydrogen atom by coherent population transfer from the initial S-state to an excited D-state via the p-continuum and further ionization into the f-continuum states. A direct optimization procedure is used to find a domain of laser parameters, for which the efficiency of the control with respect to the time delay and energy detuning between the laser pulses is maximized.

 This article features online multimedia enhancements

(Some figures in this article are in colour only in the electronic version)

1. Introduction

The coupling of a continuum to a discrete state by a strong laser field forms so-called ‘laser-induced continuum structures’ (LICS). In photoionization studies, LICS manifest themselves as autoionization-like resonances in various observable quantities. The LICS phenomenon was theoretically predicted in the mid 1970s [1, 2], and it was later observed, e.g., in the rotation of the polarization of transmitted light [3], third harmonic generation [4, 5], in the integral and partial photoionization cross sections of a number of atoms [6–13] and in the molecular ionization continuum [14]. LICS are studied in the contexts of population trapping and population transfer via the continuum [15], atomic stabilization [16] and other coherent control phenomena. Various aspects of the LICS phenomenon are described, for example, in [17–22].

To date only very little is known about vector correlations in the region of LICS: the vast majority of previous publications deal with integral and hence angle-independent characteristics. There are a few theoretical papers on the angular distribution [23–25] and

the spin polarization [26–28] of photoelectrons in the region of LICS, but more effort is needed to achieve a better understanding of the basic features. In particular, we are not aware of such studies in the femtosecond time domain. With the advent of bright VUV and soft x-ray radiation sources (free-electron lasers, lasers based upon high-harmonic generation, or next-generation synchrotrons) and more efficient electron detectors, such experiments are just becoming feasible.

More than a decade ago it was suggested that the control of the photoelectron angular distribution (PAD) can be achieved by manipulating a system with two interfering ionization paths [29, 30]. In remarkable studies with Rydberg states of calcium [31–33], the control was demonstrated by the time delay of a second ionizing pulse over the ejected-electron angular distribution in the region of a ‘natural’ autoionizing state due to quantum-mechanical coherence in the intermediate wavepacket representing the laser-excited state. The influence of LICS on the PAD raises a question about the possibility of controlling the PAD by manipulating the LICS. Indeed, Nakajima and Buica [24, 25] predicted recently that the PAD formed by the probe radiation can be controlled by generating LICS: a dressing laser, coupling the $(6p)^2P$ discrete state of potassium to the continuum, can modify the branching ratio of ionization into the *s*- and *d*-continua. This causes changes in the PAD formed by ionization from the $(4p)^2P$ excited potassium state. The predictions of [24, 25] were made for sufficiently long, nanosecond, laser pulses, and the PADs were supposed to be controlled by the two-photon frequency detuning and the polarization of the dressing laser.

In the present paper we consider a different PAD controlling scheme: an initial atomic *S*-state is ionized by a probe laser pulse into the *p*-continuum. The control of the PAD is achieved by coupling the *p*-continuum to a discrete *D*-state by a dressing field, which generates LICS and switches on the *f*-ionization channel through coherent population transfer (a two-photon Raman transition) [15, 34] from the initial *S*-state to the excited *D*-state via the LICS. The interplay between the outgoing photoelectron *p*- and *f*-waves, each individually characterized by a specific angular distribution, depends upon the details of the laser pulses. The entire process represents an example of coherent phase control in a bichromatic electromagnetic field [35].

We focus on the femtosecond time domain and, therefore, solve the time-dependent Schrödinger equation (TDSE) directly on a spacetime grid. This avoids possible restrictions due to the pulse duration and strength imposed by rotating-wave or adiabatic approximations. As a by-product of our calculations, we gain access to the motion of the electron cloud, which allows us to visualize the dynamics of the process. Using hydrogen in this, our first paper, has the advantages that (i) the calculations are exact within the numerical accuracy and (ii) the effects under investigation are not obscured by multi-electron dynamics.

An important tool of the present study is the direct optimization of the laser-pulse parameters [36] used to find frequency and time domains, in which the effect of the LICS on the PAD is maximized. This goal is achieved by constructing and then optimizing the target functional, which evaluates the difference between the PADs with and without the effect of the dressing pulse.

Section 2 summarizes our theoretical approaches. The results of the calculations are presented and discussed in section 3, which is followed by some concluding remarks.

2. Methods of calculation

2.1. Electromagnetic fields

Figure 1 displays the level scheme and driving fields for the hydrogen atom. We take the pulsed, linearly polarized bichromatic electromagnetic field in the form

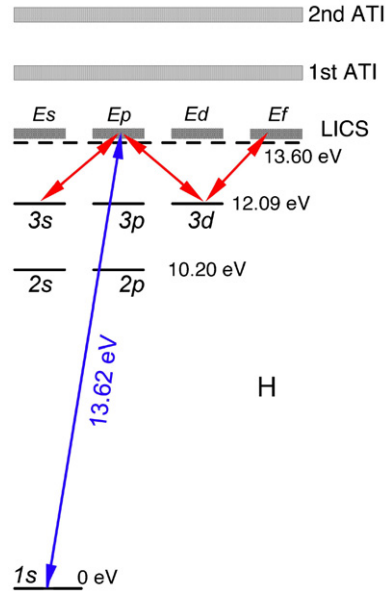


Figure 1. Hydrogen energy levels and scheme of the driving fields. The positions of LICS and the first two ATI peaks are indicated.

$$E(t) = E_d(t) \sin(\omega_d t + \phi_d) + E_p(t) \sin(\omega_p t + \phi_p), \quad (1)$$

where the low-frequency IR dressing ('d') and the high-frequency VUV probe ('p') fields are described by the carrier frequencies ω_d , ω_p , the phases ϕ_d , ϕ_p and the envelopes $E_d(t)$, $E_p(t)$, respectively. The envelope functions are taken in the Gaussian form

$$E_i(t) = E_i^0 \exp[-(t - \tau_i)^2 / T_i^2], \quad (i = d, p) \quad (2)$$

for $\tau_i - 3T_i < t < \tau_i + 3T_i$ and $E_i(t) = 0$ otherwise. Here E_i^0 is the field amplitude, T_i characterizes the time width of the pulse, and τ_i is the time of the pulse maximum. The duration and peak intensities of the probe and dressing fields are fixed during the present study, while the controlling parameters are the two-photon detuning

$$\Delta\omega = (\omega_p - \omega_d) - (E_{n=3} - E_{1s}) \quad (3)$$

and the time delay between the probe and the dressing pulses

$$\Delta t = \tau_p - \tau_d. \quad (4)$$

We apply fields with peak intensities of $I_p = 10^{10} \text{ W cm}^{-2}$ ($E_p^0 = 5.338 \times 10^{-4} \text{ au}$) and $I_d = 10^{12} \text{ W cm}^{-2}$, respectively. These moderate field intensities are used to unambiguously demonstrate the proposed controlling mechanism: for higher intensities, multiphoton ionization and competing tunnelling ionization can yield more complex PADs and mask the effect. In the present calculations, only a few atoms, namely less than 10^{-3} of the initial ground state population, is transferred to other states and the continuum during the action of the fields.

The pulse durations are fixed at $T_p = T_d = 20 \text{ fs}$, corresponding to 33.3 fs for the full-width half-maximum (FWHM) of the pulses and their bandwidth of 0.02 eV. For time-independent ϕ_d and ϕ_p , we checked that the phase effects are negligible due to the large number of optical cycles in the pulses [37]. However, the relative phase of the two pulses

could be important if the probe field is a harmonic of the dressing field (see, for example, [29, 38]).

The carrier frequencies ω_p and ω_d and the time delay Δt were varied in a selected domain. This domain was chosen in accordance with the optimization procedure described in section 2.3 below.

2.2. Wavepacket approach

We solve the TDSE with the Hamiltonian $H(\mathbf{r}, t)$ of the hydrogen atom interacting with linearly polarized radiation (in atomic units),

$$H(\mathbf{r}, t) = -\frac{\Delta}{2} - \frac{1}{r} + E(t)r \cos \vartheta, \quad (5)$$

where ϑ is the angle between the radius vector \mathbf{r} of the electron and the direction of the linear polarization (taken as the z -axis of the coordinate system). Since the duration of the atomic interaction with the laser fields is short in the present study, quantum beats due to coherent excitation of the fine-structure levels are irrelevant, and the spin and spatial parts of the wavefunction can be considered uncoupled. The TDSE is solved by the time-dependent close-coupling method (see, for example, [39–41]). In this approach, the solution is expanded in partial waves as

$$\Psi(\mathbf{r}, t) = \frac{1}{r} \sum_{\ell=0}^{\infty} \xi_{\ell}(r, t) \sqrt{\frac{2\ell+1}{4\pi}} P_{\ell}(\cos \vartheta), \quad (6)$$

where $P_{\ell}(x)$ is a standard Legendre polynomial. We then solve the set of coupled equations for the radial functions $\xi_{\ell}(r, t)$,

$$i \frac{\partial \xi_{\ell}(r, t)}{\partial t} = \left[-\frac{1}{2} \frac{\partial^2}{\partial r^2} + \frac{\ell(\ell+1)}{2r^2} - \frac{1}{r} \right] \xi_{\ell}(r, t) + r E(t) \frac{1}{3} \sum_{\ell'=\ell\pm 1} v_{\ell\ell'}^1 \xi_{\ell'}(r, t). \quad (7)$$

Here $v_{\ell\ell'}^L = v_{\ell'\ell}^L = \sqrt{(2\ell+1)(2\ell'+1)} (\ell 0, \ell' 0 | L 0)^2$ with $(\ell 0, \ell' 0 | L 0)$ denoting a Clebsch–Gordan coefficient. The set (7) is truncated at $\ell = \ell_{\max}$ and has to be solved with the initial condition $\xi_{\ell}(r, 0) = \delta_{\ell 0} P_{1s}(r)$, where $P_{1s}(r)$ is the 1s electron radial wavefunction of atomic hydrogen.

The eigenfunction of the atomic Hamiltonian, corresponding to the photoelectron propagating with linear momentum \mathbf{k} , is also expanded in partial waves as

$$\Phi_{\mathbf{k}}^{-}(\mathbf{r}) = \frac{4\pi}{r} \sum_{\ell m} i^{\ell} e^{-i\delta_{\ell\ell}} P_{\ell\ell}(r) Y_{\ell m}^{*}(\Theta, \Phi) Y_{\ell m}(\vartheta, \varphi), \quad (8)$$

where the angles $\{\Theta, \Phi\}$ characterize the direction of \mathbf{k} , $P_{\ell\ell}(r)$ is the energy-normalized regular Coulomb function, and $\delta_{\ell\ell} = \arg \Gamma(\ell+1 - i/k)$ is the scattering Coulomb phase. The probability density for finding the photoelectron with energy $\varepsilon = k^2/2$ emitted in the direction $\Omega_{\mathbf{k}}$ is given by

$$\frac{d^2 \mathcal{P}}{d\varepsilon d\Omega_{\mathbf{k}}} = \lim_{t \rightarrow \infty} |\langle \Phi_{\mathbf{k}}^{-}(\mathbf{r}) | \Psi(\mathbf{r}, t) \rangle|^2 = \frac{\mathcal{P}_{\varepsilon}}{4\pi} \left[1 + \sum_{L>0} \beta_L(\varepsilon) P_L(\cos \Theta) \right]. \quad (9)$$

Here $\mathcal{P}_{\varepsilon}$ is the angle-integrated probability density (i.e., the photoelectron energy spectrum)

$$\mathcal{P}_{\varepsilon} = \int d\Omega_{\mathbf{k}} \frac{d^2 \mathcal{P}}{d\varepsilon d\Omega_{\mathbf{k}}}. \quad (10)$$

The anisotropy parameters, $\beta_L(\varepsilon)$ (below we will omit the argument ε), are given by

$$\beta_L = \frac{1}{\mathcal{P}_\varepsilon} \sum_{\ell\ell'} i^{\ell'-\ell} e^{i(\delta_{\varepsilon\ell}-\delta_{\varepsilon\ell'})} v_{\ell\ell'}^L Z_{\varepsilon\ell} Z_{\varepsilon\ell'}^*, \quad (11)$$

where

$$Z_{\varepsilon\ell} = \lim_{t \rightarrow \infty} \int_0^\infty P_{\varepsilon\ell}(r) \xi_\ell(r, t) dr, \quad (12)$$

so that

$$\mathcal{P}_\varepsilon = \sum_\ell |Z_{\varepsilon\ell}|^2. \quad (13)$$

To solve equation (7) numerically, we use the symmetric split-operator algorithm [42–44] in combination with the Crank–Nicolson propagator and the Caley approximation [45, 46]. A complex potential (gobbler) is introduced at large distances to avoid unphysical reflections. Similar recipes are widely used in the literature (see, for example, [40, 41, 47, 48]) and hence will not be described in more detail here.

We checked the stability and accuracy of our results with respect to changing the spacetime grid, the propagation distance, the radius and type of the gobbler and the number of coupled channels. The results for the principal photoelectron line were obtained with a spatial step of $0.010\text{--}0.015a_0$ (where a_0 denotes the Bohr radius), a time step of 0.02 atomic units ($1 \text{ au} = 24.19$ attoseconds), inner gobbler radii of $1500\text{--}2000a_0$, and $\ell_{\max} = 15\text{--}20$. Using appropriate initial data, we tested the code by reproducing the hydrogen photoelectron spectra and the time-dependent level populations of [49].

2.3. Direct optimization procedure

The direct solution of the TDSE is time-consuming. Therefore, to find a domain for the pulse parameters ($\omega_p, \omega_d, \Delta t$) with the most pronounced controlling effect on the PAD, we directly optimized the laser parameters based upon the close-coupling method. In this procedure, the wavefunction of the system is expanded in the basis of the orthogonal and normalized unperturbed atomic wavefunctions of the discrete and continuum states as

$$\Psi(\mathbf{r}, t) = \sum_{n\ell} a_{n\ell}(t) \psi_{n\ell}(\mathbf{r}) e^{-i\varepsilon_{n\ell}t} + \sum_\ell \int b_{\varepsilon\ell}(t) \psi_{\varepsilon\ell}(\mathbf{r}) e^{-i\varepsilon t} d\varepsilon, \quad (14)$$

where $\psi_{n\ell}(\mathbf{r})$ and $\psi_{\varepsilon\ell}(\mathbf{r})$ are the corresponding stationary-state wavefunctions while $\varepsilon_{n\ell}$ and ε stand for the energies of the discrete states and the continuum, respectively. Substituting the close-coupling ansatz (14) back into the TDSE yields the following coupled sets of equations for the amplitudes $a_{n\ell}(t)$ and $b_{\varepsilon\ell}(t)$:

$$i \frac{da_{n\ell}(t)}{dt} = E(t) \left[\sum_{n'\ell'} U_{n\ell n'\ell'} e^{i(\varepsilon_{n\ell}-\varepsilon_{n'\ell'})t} a_{n'\ell'}(t) + \sum_{\ell'} \int U_{n\ell m\ell'}(\varepsilon) e^{i(\varepsilon_{n\ell}-\varepsilon)t} b_{\varepsilon\ell'}(t) d\varepsilon \right], \quad (15)$$

$$i \frac{db_{\varepsilon\ell}(t)}{dt} = E(t) \left[\sum_{n'\ell'} U_{\ell n'\ell'}(\varepsilon) e^{i(\varepsilon-\varepsilon_{n'\ell'})t} a_{n'\ell'}(t) + \sum_{\ell'} \int U_{\ell\ell'}(\varepsilon, \varepsilon') e^{i(\varepsilon-\varepsilon')t} b_{\varepsilon'\ell'}(t) d\varepsilon' \right]. \quad (16)$$

Here $U_{n\ell n'\ell'}$, $U_{n\ell\ell'}(\varepsilon)$ and $U_{\ell\ell'}(\varepsilon, \varepsilon')$ are bound–bound, bound–free and free–free dipole matrix elements.

The free–free matrix elements (i.e., the second sum in equation (16)) correspond to the rescattering process, which is crucial for the correct description of the photoelectron spectrum

at high energies [50–53]. However, the effects considered in the present paper relate to the main photoelectron peak at low energies, and hence we neglect these matrix elements in our calculations.

Comparison of the photoelectron spectra calculated for photoionization of hydrogen by a linearly polarized laser field with frequency 2 eV, intensity $4 \times 10^{14} \text{ W cm}^{-2}$ and full duration of 5 fs [57, 59] shows that deformation of the spectra due to free–free transitions is two orders of magnitude lower than structures caused by bound–free transitions. To further estimate the errors caused by neglecting the free–free transitions in the general case, one needs to analyse the formation of the above-threshold ionization (ATI) peaks. These peaks are formed by two processes: bound–free transitions [57, 59] and free–free transitions [54–56]. Contributions from both types of transitions depend on how rapidly the bound–free matrix element decreases when the free-electron energy increases. The effect of bound–free transitions dominates at low energies. Hence, if the laser frequency is sufficiently low, the first few ATI peaks are formed mostly by bound–free transitions. At high energies, however, the effect of free–free transitions dominates due to the rescattering process [50–53].

In most applications when the method described here is used, and particularly in the present work, the intensity of the field is relatively low, so that the portion of the probability density that forms the ATI peaks itself is much smaller than the portion that forms the main peaks. In those cases, the approximation is valid.

Since only qualitative results from the direct optimization approach are needed in the present study, we retain in expansion (14) a small number of discrete hydrogen states (up to principal quantum number $n = 3$) as well as the continuum states ($\varepsilon s, \varepsilon p, \varepsilon d, \varepsilon f$). The close-coupling equations are then solved without discretization of the continuum, by employing an approach based upon the general properties of the time-dependent integral equations. Further details are described in [57–59].

To find a domain of the carrier frequencies ω_d, ω_p and the time delay Δt , in which maximum changes in the PAD are expected with respect to the unperturbed angular distribution, we construct the following target functional:

$$J = \int_0^\pi \sin \Theta \, d\Theta (f(\Theta) - \cos^2 \Theta)^2. \quad (17)$$

Here $f(\Theta)$ is the energy integrated PAD

$$f(\Theta) = N_f \int d\varepsilon \left| \sum_{\ell} b_{\varepsilon\ell}^* \cdot i^{\ell} e^{-i\delta_{\varepsilon\ell}} \sqrt{\frac{2\ell+1}{4\pi}} P_{\ell}(\cos \Theta) \right|^2, \quad (18)$$

where the time-independent coefficients $b_{\varepsilon\ell}$ denote the limit of the $b_{\varepsilon\ell}(t)$ coefficients at the end of both pulses. Furthermore, the normalization coefficient N_f is adjusted to ensure that $f(0) = 1$. In our case the dominating contribution in the energy integrated PAD (18) comes from the main photoline. The term $\cos^2 \Theta$ in equation (17) represents the unperturbed PAD in the main photoline, generated by the probe pulse.

By solving the set of equations (15) and (16), the integrated PAD (18) and the target functional (17) are determined as functions of the laser pulse parameters. To find the maximum of the functional, the conjugate gradient search method [46] was used. The gradient of the target functional with respect to the laser parameters was calculated numerically using the finite-difference approximation. The optimizations with respect to the frequencies ω_d and ω_p , as well as the time delay Δt , were performed separately at each iteration step of the direct optimization procedure.

The direct optimization pointed unambiguously towards a scenario, in which the maximum controlling effect should be expected for ω_p just above the ionization threshold of hydrogen

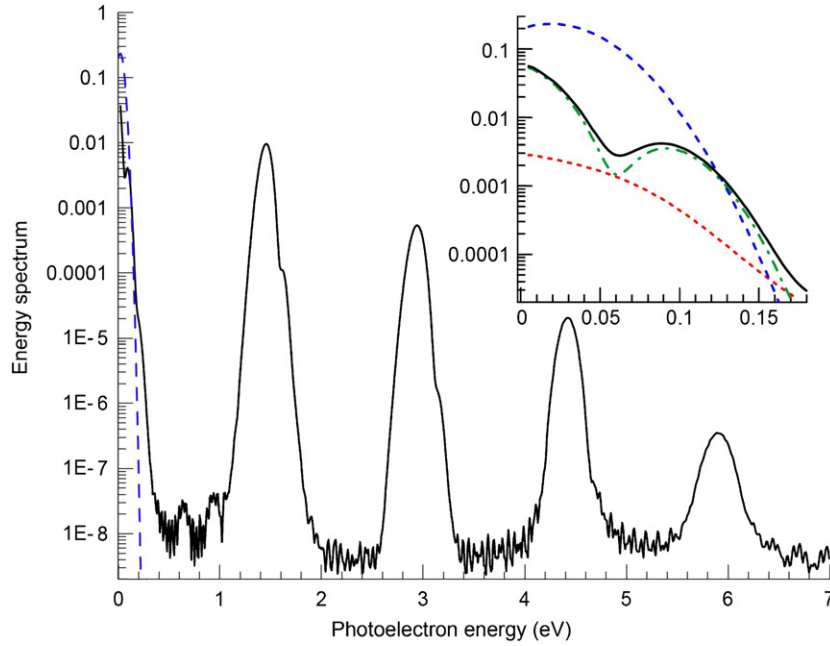


Figure 2. Photoelectron spectra. Solid line: the dressing ($\omega_d = 1.492$ eV) and the probe ($\omega_p = 13.617$ eV) pulses coincide in time ($\Delta t = 0$) with the detuning (3) $\Delta\omega = 0.038$ eV. Dashed line: without the dressing field. The inset shows the near-threshold regime with partial contributions from p (chain curve) and f (dotted curve) channels.

and ω_d just below the ionization threshold for the 3d state. The situation could be different for other atoms and will be explored in future work.

3. Results and discussion

To illustrate the controlling effect of LICS on the PAD, we now turn to the region identified in section 2.3, i.e., we fix the carrier frequency of the probe pulse to $\omega_p = 13.617$ eV, which is 0.019 eV above the ionization threshold⁴. Note that modern electron position-sensitive detectors can measure angular distributions of photoelectrons with energy less than 0.1 eV, even down to a few meV, without losing relative energy resolution [60].

Typical calculated photoelectron spectra are displayed in figure 2. The energy spectrum (see equations (10) and (13)) is normalized to unity when integrated over the continuum and summed over the hydrogen bound states, including the ground state. The spectrum contains a set of the above-threshold ionization (ATI) peaks, produced by the probe photon, together with an integer number of photons of the dressing field. Note the ‘numerical noise’ at the level of 10^{-8} , which is sensitive to the details of the grid and the gobble; for the present calculations we did not need to improve the accuracy further. The inset in figure 2 exhibits the near-threshold energy region with the first resonance. The spectrum produced by a single probe pulse is shown for comparison. Note that part of the line is hidden below the ionization threshold, corresponding to photoexcitation of high Rydberg states.

⁴ At energies this close to threshold, the ‘atomic units’ used in our equations imply the reduced mass of the electron, which is 0.999 456 of the electron’s rest mass. The unit of energy is 27.197 eV, the ionization threshold of hydrogen is 13.598 eV, and $E_{3n} = 12.087$ eV.

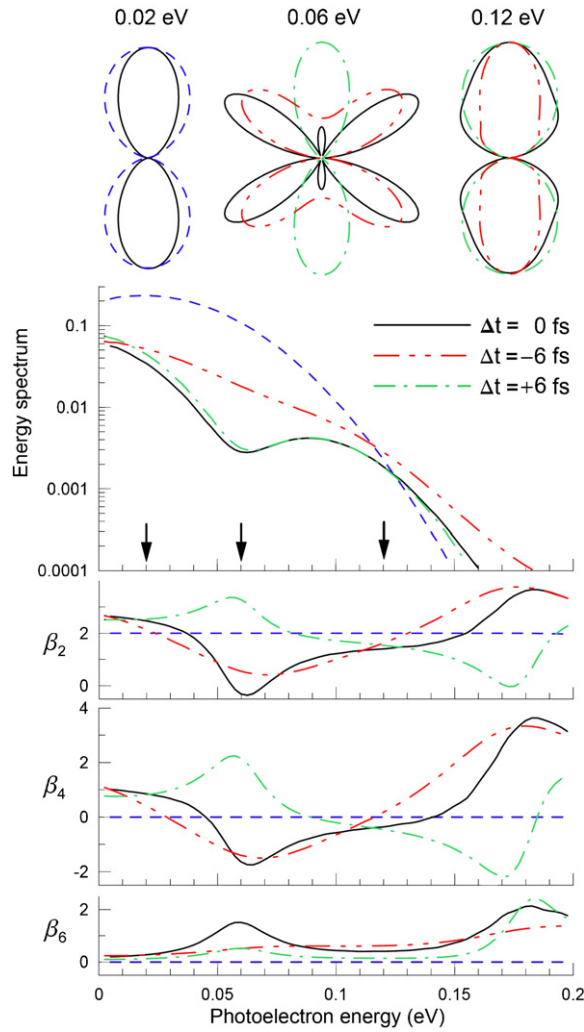


Figure 3. Photoelectron spectrum and energy dependence of the anisotropy parameters in the region of the main resonance structure for fixed detuning $\Delta\omega = 0.038$ eV ($\omega_p = 13.617$ eV, $\omega_d = 1.492$ eV) and various time delays $\Delta t = \tau_p - \tau_d$. Dashed line: without the dressing pulse. The polar plots show the PADs for various choices of Δt at photoelectron energies of 0.02 eV, 0.06 eV and 0.12 eV, which are marked by arrows on the energy axis.

The line is formed by the p-wave photoelectrons. Switching on the dressing field leads to formation of LICS in the region of the photoline, due to mixing of 3s and 3d states with εp and εf continua. The decrease of the ionization probability after switching on the dressing field is mainly due to two reasons: (i) a population transfer to the excited 3s and 3d states via the continuum and (ii) the ponderomotive shift of the ionization threshold (~ 0.06 eV in the field maximum) during the action of the dressing pulse. An additional structure appears due to interference of ionization pathways from the 3s and 3d hydrogenic states into the εp continuum. As seen in the inset of figure 2, after switching on the dressing field, the p-wave of the photoelectron keeps dominating almost within the entire first resonance, but the contributions from the f-wave are not negligible, especially taking into account the interference terms in

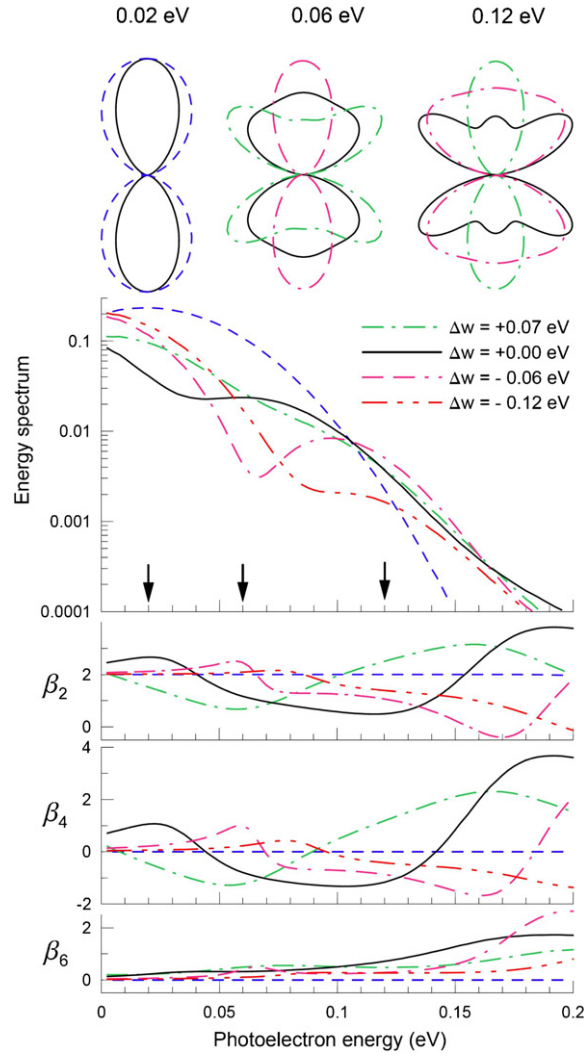


Figure 4. Same as figure 3 but for fixed time delay $\Delta t = -9$ fs and various detunings $\Delta\omega$. The carrier frequency of the probe is fixed at 0.019 eV above the ionization threshold ($\omega_p = 13.617$ eV, $\omega_d = 1.530$ eV $-\Delta\omega$).

the PAD according to equations (9) and (11). Note that although p-wave photoelectrons are produced from the 3d-state as well, the projection of their angular momentum on the z -axis is zero and hence yields the same $\cos^2 \Theta$ -type PAD as the photoelectrons ejected from the ground state.

Figure 3 shows variations of the photoelectron energy spectrum and the anisotropy coefficients β_L in the region of the main resonance structure when the time delay Δt for fixed carrier frequency ω_d is changed, i.e., for fixed detuning $\Delta\omega$. Figure 4 shows similar variations for a fixed time delay $\Delta t = -9$ fs when the frequency of the dressing laser ω_d is changed. The values of the fixed parameters, $\Delta\omega$ and Δt , in figures 3 and 4, respectively, are close to one of the optimal sets of values found by the direct optimization procedure described in section 2.3.

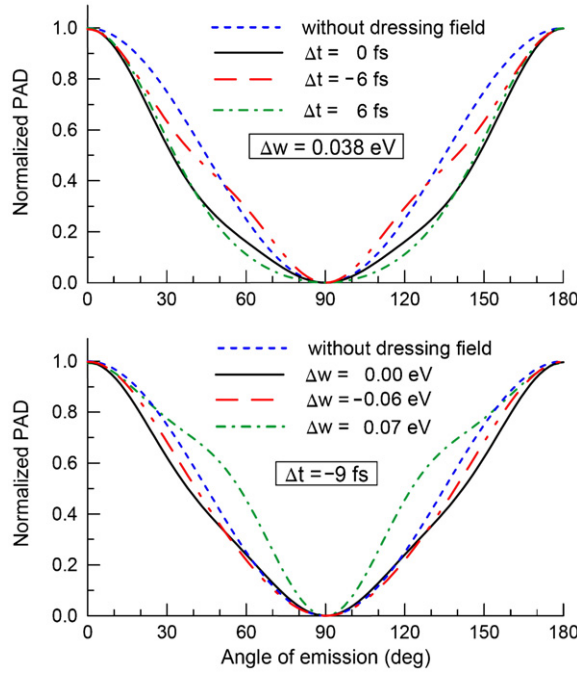


Figure 5. Photoelectron angular distributions, averaged over the resonance, for different Δt at fixed $\Delta\omega = 0.038$ eV (upper panel) and for different $\Delta\omega$ at fixed $\Delta t = -9$ fs (lower panel). The curves are the same as in figures 3 and 4, respectively.

The anisotropy parameters β_L with odd L are not presented because of their small values ($\lesssim 0.01$). This corresponds to an almost ideal ‘forward–backward’ symmetry of the angular distributions of the photoelectrons due to the large number of optical cycles within the pulses and the insensitivity of the results to the relative phase of the probe and dressing fields, as indicated in section 2.1.

The anisotropy parameters assume constant values, $\beta_2 = 2$ and $\beta_L = 0$ for $L \neq 2$, if only the probe field operates. When the dressing pulse is switched on, the β_L parameters exhibit sharp energy variations even within the width of the resonance. The parameter β_6 of equation (11) is non-zero only due the contribution from the f wave, while both waves, p and f, affect the β_2 and β_4 parameters, including the interference between the two waves. The anisotropy parameters are not independent of each other. This is clearly seen when comparing the energy dependence of the β_2 and β_4 parameters. To explain this correlation, we note that only two partial waves, p and f, dominate the final continuum wavefunction (6) in the main resonance structure. Therefore, from equations (6), (8) and (9),

$$\frac{d^2 \mathcal{P}}{d\varepsilon d\Omega_k} \sim |B_1 P_1(\cos \Theta) + B_3 P_3(\cos \Theta)|^2. \quad (19)$$

The angular distribution (19) vanishes at $\Theta = 90^\circ$. At the same time it is described by the sum (9) with $L = 2, 4, 6$. Hence, a relation between the anisotropy parameters β_L follows. Specifically, we find

$$\beta_2 - \frac{3}{4}\beta_4 + \frac{5}{8}\beta_6 = 2. \quad (20)$$

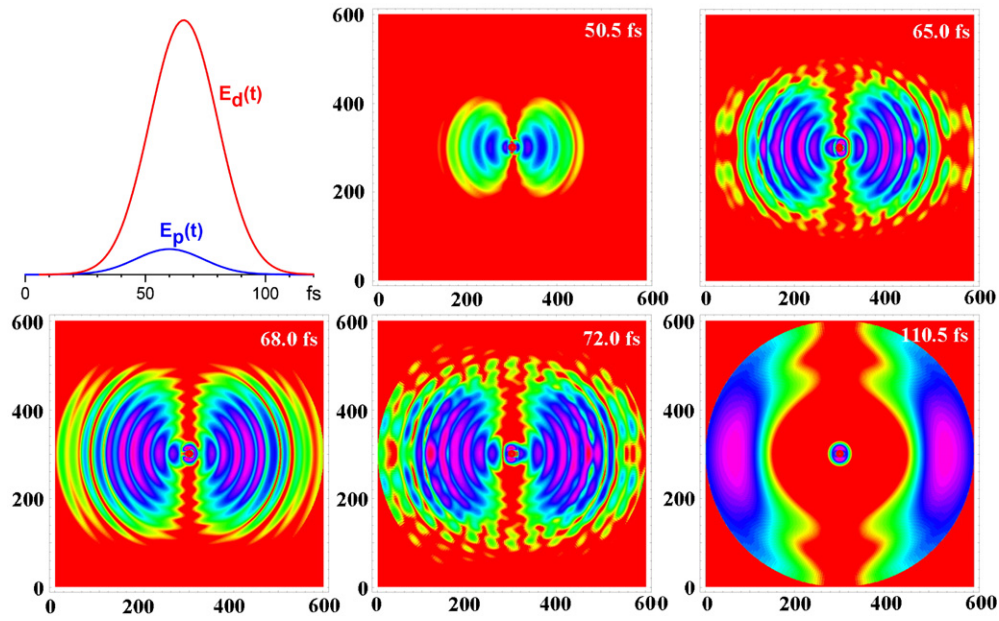


Figure 6. Snapshots of the photoelectron density at times 50.5 fs, 65.0 fs, 68.0 fs, 72.0 fs and 110.5 fs, for the pulses with $\Delta t = -6$ fs and $\Delta\omega = 0.038$ eV ($\omega_p = 13.617$ eV, $\omega_d = 1.492$ eV). The top left panel shows the envelopes of the probe, $E_p(t)$, and dressing, $E_d(t)$, fields. The electric field vectors are horizontal. The contour plots cover the range of electron densities from 10^{-13} to $10^{-18.5}$ on a logarithmic scale over a square of side $600a_0$ with the hydrogen nucleus in the centre.

The curves in figures 3 and 4 supply data for the calculation of the PAD at any energy within the range of interest and accounting for a finite energy resolution. As examples, in the upper part of figures 3 and 4 polar plots of the PAD are displayed for selected photoelectron energies. They visualize sharp changes of the PAD within the resonance structure and changes of the PAD achieved by manipulating the LICS in the time and frequency domains, i.e., by changing the time delay Δt and the detuning $\Delta\omega$ of the dressing field. After averaging over the entire resonance, the control effect is still pronounced (see figure 5), but less dramatic.

It is worth noting that similar variations of the PAD were obtained in the close-coupling calculations discussed in section 2.3, in which the Rydberg states were not taken into account. This points to the fact that the PAD variations are mainly caused by transitions involving the continuum, rather than by stimulated Raman transitions involving the Rydberg states of hydrogen.

Figure 3 contains another interesting result: in spite of the very similar total cross sections for $\Delta t = 0$ fs and $\Delta t = +6$ fs, the corresponding angular distributions are very different. This indicates a crucial role of the interference between p and f outgoing electron waves in the formation of the PAD.

The interference between the p- and f-waves is barely seen in the snapshots (figure 6) of the photoelectron wavepackets at different times during the photoionization process, although the pulse parameters are close to the optimal values for altering the PAD. The electron density in the snapshots is a photoelectron-energy-integrated image with the dominating contribution from the p-wave and a significant contribution from the first ATI peak (see figure 2) originating from the d- and s-waves. The latter are seen in the directions normal to the electric field vector in

the snapshots for 65.0 fs and 72.0 fs, while the p-electrons from different ionization pathways produce a strong interference in the forward and backward directions. The supplemental movie, available from stacks.iop.org/JPhysB/39/4659, illustrates the rapid changes of the electron density pattern on a scale of hundreds of attoseconds, in accordance with the frequencies of the applied fields. The movie covers the time interval from 15.5 fs to 116.0 fs, counting from the beginning of the first (probe) pulse, as indicated at the top left of figure 6, with a time step of 0.5 fs between two successive frames.

4. Summary and conclusions

We considered theoretically the control of the photoelectron angular distribution in atomic photoionization, generated by a femtosecond probe pulse, by changing the time delay and detuning of a dressing pulse, which induces a continuum structure in the region of the photoelectron line. The controlling effect occurs due to the population transfer, by the dressing field, into a new continuum opened by the laser-induced continuum structure and a related discrete state. While the effect was demonstrated for the hydrogen atom, it is expected to be of a general nature. A well-pronounced effect was observed in the femtosecond time domain with moderately strong fields. The planned extension of the present analysis to other atoms will yield more information on the effect, as well as the possibilities of its experimental verification.

Acknowledgments

The authors would like to dedicate this paper to the memory of the late Professor Leonid P Presnyakov, who had a vital impact on linking the wavepacket and direct optimization methods. We also thank M Meyer, S I Strakhova, N M Kabachnik and A Huetz for fruitful discussions. This work was supported, in part, by the Russian Foundation for Basic Research under projects no 04-02-17236 (ANG) and no 06-02-17089 (ADK), and by the United States National Science Foundation under grant PHY-0244470 (KB). Finally, ANG gratefully acknowledges the hospitality of Drake University during his visit, when this work was initiated.

References

- [1] Armstrong L Jr, Beers B L and Feneuille S 1975 *Phys. Rev. A* **12** 1903
- [2] Heller Yu I and Popov A K 1976 *Opt. Commun.* **18** 449
- [3] Heller Yu I, Lykinykh V F, Popov A K and Slabko V V 1981 *Phys. Lett. A* **82** 4
- [4] Pavlov L I, Dimov S S, Metchkov D I, Mileva G M, Stamenov K V and Altschuller G B 1982 *Phys. Rev. A* **89** 441
- [5] Dimov S S, Pavlov L I, Stamenov K V, Heller Y I and Popov A K 1983 *Appl. Phys. B* **30** 35
- [6] Shao Y L, Charalambidis D, Fotakis C, Zhang J and Lambropoulos P 1991 *Phys. Rev. Lett.* **67** 3669
- [7] Cavalieri S, Pavone F S and Matera M 1991 *Phys. Rev. Lett.* **67** 3673
- [8] Cavalieri S, Matera M, Pavone F S, Zhang J, Lambropoulos P and Nakajima T 1993 *Phys. Rev. A* **47** 4219
- [9] Eramo R, Cavalieri S, Fini L, Matera M and DiMauro L F 1997 *J. Phys. B: At. Mol. Opt. Phys.* **30** 3789
- [10] Cavalieri S, Eramo R, Fini L, Materazzi M, Faucher O and Charalambidis D 1998 *Phys. Rev. A* **57** 2915
- [11] Halfmann T, Yatsenko L P, Shapiro M, Shore B M and Bergmann K 1998 *Phys. Rev. A* **58** R46
- [12] Yatsenko L P, Halfmann T, Shore B M and Bergmann K 1999 *Phys. Rev. A* **59** 2926
- [13] Bohmer K, Halfmann T, Yatsenko L P, Charalambidis D, Horsmans A and Bergmann K 2002 *Phys. Rev. A* **66** 013406
- [14] Faucher O, Hertz E, Lavorel B, Chaux R, Dreier T, Berger H and Charalambidis D 1999 *J. Phys. B: At. Mol. Opt. Phys.* **32** 4485

- [15] Paspalakis E, Protopapas M and Knight P L 1998 *J. Phys. B: At. Mol. Opt. Phys.* **31** 775
- [16] Fedorov M V and Poluektov N P 2004 *Phys. Rev. A* **69** 033404
- [17] Heller Y I and Popov A K 1981 *Laser Induction of Nonlinear Resonances in Continuous Spectra* (Novosibirsk: Nauka) (in Russian)
- [18] Fedorov M V and Kazakov A E 1989 *Prog. Quantum Electron.* **13** 1
- [19] Knight P L, Lauder M A and Dalton B J 1990 *Phys. Rep.* **190** 1
- [20] Magunov A I, Rotter I and Strakhova S I 2001 *J. Phys. B: At. Mol. Opt. Phys.* **34** 29
- [21] Vitanov N V, Halfmann T, Shore B W and Bergmann K 2001 *Ann. Rev. Phys. Chem.* **52** 763
- [22] Popov A K, Kimberg V V and George T F 2004 *Phys. Rev. A* **69** 043816
- [23] Magunov A I, Rotter I and Strakhova S I 2002 *Laser Phys.* **12** 429
- [24] Nakajima T and Buica G 2005 *Phys. Rev. A* **71** 013413
- [25] Buica G and Nakajima T 2005 *Phys. Rev. A* **72** 053416
- [26] Andryushin A I and Fedorov 1978 *Zh. Eksp. Teor. Fiz.* **75** 2037
Andryushin A I and Fedorov 1978 *Sov. Phys.—JETP* **48** 228
- [27] Alber G and Zoller P 1983 *Phys. Rev. A* **27** 1713
- [28] Nakajima T and Nikolopoulos A A 2003 *Phys. Rev. A* **68** 013413
- [29] Yin Y-Y, Chen C and Elliott D S 1992 *Phys. Rev. Lett.* **69** 2353
- [30] Wang F, Chen C and Elliott D S 1996 *Phys. Rev. Lett.* **77** 2416
- [31] van Leeuwen R, Bajema M L and Jones R R 1999 *Phys. Rev. Lett.* **82** 2852
- [32] van Leeuwen R, Vijayalakshmi K and Jones R R 2001 *Phys. Rev. A* **63** 033403
- [33] Bajema M L, Jones R R and Gallagher T F 2004 *Phys. Rev. A* **70** 062722
- [34] Bergmann K, Thener H and Shore B W 1998 *Rev. Mod. Phys.* **70** 1003
- [35] Ehloltzky F 2001 *Phys. Rep.* **345** 175
- [36] Kondorskiy A 2005 *Proc. of the 24th Int. Conf. on Photonic, Electronic and Atomic Collisions (Rosario, Argentina)* ed R Rivarola, M A P Lima, J E Miraglia and E C Montenegro (Singapore: World Scientific)
- [37] Cormier E and Lambropoulos P 1998 *Eur. Phys. J. D* **2** 15
- [38] Schafer K J and Kulander K C 1992 *Phys. Rev. A* **45** 18026
- [39] LaGatutta K J 1990 *Phys. Rev. A* **41** 5110
- [40] Rose-Franco L, Sanpera A, Pons M L and Plaja L 1991 *Phys. Rev. A* **44** 4652
- [41] Krause J L, Schafer K J and Kulander K C 1992 *Phys. Rev. A* **45** 4998
- [42] Fleck J A Jr, Morris J R and Feit M D 1976 *Appl. Phys.* **10** 129
- [43] Feit M D, Fleck J A Jr and Steiger J A 1982 *J. Comput. Phys.* **47** 412
- [44] Hermann M R and Fleck J A Jr 1988 *Phys. Rev. A* **38** 6000
- [45] McCullough E A and Wyatt R E 1971 *J. Chem. Phys.* **54** 3578
- [46] Press W H, Teukolsky S A, Vetterling W T and Flannery B P 2001 *Numerical Recipes in Fortran 77: The Art of Scientific Computing* vol 1 2nd edn (Cambridge: Cambridge University Press)
- [47] Kazansky A K 1998 *J. Phys. B: At. Mol. Opt. Phys.* **31** L579
- [48] Kazansky A K and Kabachnik N M 2005 *Phys. Rev. A* **72** 052714
- [49] Gajda M, Krzywiński J, Pluciński Ł and Piraux B 2000 *J. Phys. B: At. Mol. Opt. Phys.* **33** 1271
- [50] Paulus G G, Becker W, Nickich W and Walther H 1994 *J. Phys. B: At. Mol. Opt. Phys.* **27** L703
- [51] Paulus G G, Zacher F, Walther H, Lohr A, Becker W and Kleber M 1998 *Phys. Rev. Lett.* **80** 484
- [52] Corkum P 1993 *Phys. Rev. Lett.* **71** 1994
- [53] Schafer K J, Yang B, DiMauro L F and Kulander K C 1993 *Phys. Rev. Lett.* **70** 1599
- [54] Dionissopoulou S, Mercouris Th, Lyras A, Komninos Y and Nicolaides C A 1995 *Phys. Rev. A* **51** 3104
- [55] Mercouris T, Komninos Y, Dionissopoulou S and Nicolaides C A 1996 *J. Phys. B: At. Mol. Opt. Phys.* **29** L13
- [56] Dionissopoulou S, Mercouris Th, Lyras A and Nicolaides C A 1997 *Phys. Rev. A* **55** 4397
- [57] Kondorskiy A D and Presnyakov L P 2002 *Laser Phys.* **12** 449
- [58] Kondorskiy A D and Presnyakov L P 2003 *Proc. SPIE* **5228** 394
- [59] Kondorskiy A D and Presnyakov L P 2001 *J. Phys. B: At. Mol. Opt. Phys.* **34** L663
- [60] Huetz A and Mazeau J 2000 *Phys. Rev. Lett.* **85** 530
Huetz A and Mazeau J 2000 Private communication